The equation of state of wadsleyite solid solutions: Constraining the effects of anisotropy and crystal chemistry

Supplemental Materials

Analysis of Mössbauer spectrum

To determine the ferric iron content of the wadsleyite sample, the recorded Mössbauer spectrum was fit to doublets of Lorentzian peaks using the program MossA (Prescher et al. 2012). We tested five different fitting models based on previous Mössbauer spectral analyses of wadsleyite (Mrosko et al. 2015; Kawazoe et al. 2016). For all models, conventional constraints for quadrupole doublets were applied (equal component widths and areas), with some additional constraints in some of the models: (1) two doublets in the thin approximation, one Fe^{2+} and one Fe^{3+}, constrained to have the same full width at half maximum (FWHM); (2) three doublets in the thin approximation, one Fe^{2+} and two Fe^{3+}, with Fe^{3+} doublets constrained to have the same FWHM; (3) three doublets in the thin approximation, two Fe^{2+} and one Fe^{3+}; (4) three doublets in the thin approximation, two Fe^{2+} and one Fe^{3+}, with Fe^{2+} doublets constrained to have the same FWHM; and (5) model 3, but fit with the full transmission integral. We prefer model 4 (Appendix Fig. S1, Appendix Table S2) with $Fe^{3+}/\sum Fe = 0.15(3)$. However, in terms of the ferric iron content, all models are indistinguishable within experimental uncertainty.

Fourier transform infrared absorption spectroscopy

Polarized and unpolarized infrared absorption spectra were recorded with a Bruker IFS 120 HR Fourier transform infrared (FTIR) spectrometer in a spectral range from 2500 cm^{-1} to 4000 cm^{-1} and with a resolution of 4 cm^{-1}. The light from a tungsten lamp passed through a

Michelson interferometer with a Si-coated CaF_2 beam splitter and was directed onto the single-crystal thin sections with an infrared microscope working with reflecting (Cassegranian) optics. A liquid nitrogen cooled MCT detector recorded the light transmitted through the specimen. For polarized spectra, an infrared polarizer consisting of an aluminum grating coated on KRS-5 substrate was inserted into the light path just before the sample. The spectrometer optics were constantly purged with purified H_2O and CO_2 free air. 200 scans were accumulated for each spectrum. The thin sections were laid onto a CaF_2 plate and immersed in polychlorotrifluoroethylene oil to reduce the amplitude of interference fringes resulting from internal reflections on the polished sample surfaces.

Analysis of infrared absorption spectra and calculation of hydrogen concentrations

For each crystal, we selected the spectrum less affected by interference fringes. Arising from different aperture sizes and other effects (interference, scattering, etc.), apparent background absorption was corrected for by subtracting a manually adjusted spline function. Close to absorption bands, however, we kept the background shape as simple as possible not to distort peak shapes by an uncertain extrapolation of interference fringes. A series of Gaussian functions was used to model the absorption bands. The low frequency band around 3330 cm^{-1} was fit to two peaks located at 3333 ± 3 cm^{-1} and 3343 ± 6 cm^{-1} and the high frequency band around 3600 cm^{-1} to two peaks at 3597 ± 2 cm^{-1} and 3614 ± 1 cm^{-1}. These frequencies are similar to those observed by previous FTIR studies on wadsleyite (Jacobsen et al. 2005; Deon et al. 2010; Bolfan-Casanova et al. 2012). For most spectra, an additional peak between 3449 cm^{-1} and 3484 cm^{-1} was introduced to model a weak rise in absorption at intermediate frequencies, sometimes only present as a shoulder on the strong low frequency band. In our spectra, this weak feature could equally be a remnant of interference fringes. An absorption band around 3500 cm^{-1} has been

attributed to the coupled substitution of Fe^{3+} and H^+ for Si^{4+} in wadsleyite (Bolfan-Casanova et al. 2012; Smyth et al. 2014; Kawazoe et al. 2016). Appendix Figure S3 illustrates the band analysis procedure.

From the areas beneath individual Gaussian curves, area-weighted mean wavenumbers <v> were calculated as described by Libowitzky and Rossman (1997) and the areas merged for each absorption band. The integrated absorbance A_{INT} of each band was converted to a volume concentration of H_2O equivalents using the wavenumber-dependent molar absorption coefficient for hydroxyl groups in minerals given by Libowitzky and Rossman (1997). We also applied the wadsleyite-specific molar absorption coefficient determined by (Deon et al. 2010) and found agreement between both calibrations in terms of total hydrogen concentrations. For comparison with earlier work (Kohlstedt et al. 1996; Jacobsen et al. 2005), the background corrected spectrum was scaled with the wavenumber-dependent molar absorption coefficient for hydroxyl groups as calibrated by Paterson (1982) and the resulting curve integrated in intervals spanning the range of wavenumbers where infrared absorption by hydroxyl groups has been reported for wadsleyite. This procedure again results in a volume concentration of H_2O equivalents for each spectral interval. The analysis was carried out for unpolarized spectra as well as for polarized spectra recorded at the same spot on the crystal. The results are summarized in Appendix Table S3.

Following the ideas of Libowitzky and Rossman (1996), the total absorbance A_{TOT} for an absorption band can be obtained from polarized measurements on three mutually perpendicular crystal sections. In the following, we show how the polarized spectra acquired on the two sections cut parallel to the (120) and (243) planes can be combined to a total absorbance for each section. The relations between relevant crystallographic planes and directions are illustrated in the stereographic projection of Appendix Figure S4. For the section parallel to (120), $n'_{(120)} \parallel \mathbf{c}$ and

$n''_{(120)} \parallel$ [-210]. [-210] makes an angle close to 45° to both the **a** and **b** axis. Hence, any pair of equivalent directions <210> will enclose an angle close to 90°. Therefore, the spectra collected with the electric field vector $\mathbf{E} \parallel n'_{(120)} \parallel \mathbf{c}$ and $\mathbf{E} \parallel n''_{(120)} \parallel$ [-120] suffice to model the absorbance in three nearly perpendicular planes, e.g. (120), (-120), and (001), and to calculate the total absorbance (Appendix Table S3). For the (243) section, we located the vibration directions $n'_{(243)}$ and $n''_{(243)}$ with the refractive indices at 589 nm reported by Sinogeikin et al. (1998) neglecting optical dispersion (Appendix Fig. S4). In a next step, we calculated the absorbances for two perpendicular directions lying within (243), one of them points along [-210], the other one lies in the (-120) plane. With the arguments made above for the (120) plane and the [-210] direction (and their symmetry equivalents {120} and <120>), the absorbance for $\mathbf{E} \parallel \mathbf{c}$ can be estimated. Again, the calculated absorbances along [-210] and along the **c** axis can be combined to the total absorbance (Appendix Table S3).

Dataset for the equation of state of wadsleyite solid solutions

Chemical compositions. In some studies, the ferric iron content of the iron-bearing wadsleyite sample was not determined or reported precluding calculation of the Fe_3O_4 component. The iron-bearing wadsleyites of Hazen et al. (1990), Finger et al. (1993), and Hazen et al. (2000), however, were all synthesized in rhenium capsules at similar temperatures (Finger et al. 1993) suggesting similar oxygen fugacities. Therefore, we adopt the ratio $Fe^{3+}/\Sigma Fe = z = 0.08$ determined on the sample with $x = 0.16$ by Fei et al. (1992) for the whole suite of samples studied by Hazen et al. (1990), Finger et al. (1993), and Hazen et al. (2000) except for the sample with $x = 0.395$ (Finger et al. 1993). For the wadsleyite sample of Smyth et al. (1997), the ferric iron content, $Fe^{3+}/\Sigma Fe = 0.96(5)$, was determined later by McCammon et al. (2004) and shifts the composition slightly out of the quaternary system with a maximum ratio of 2/3, i.e. as in Fe_3O_4.

Hydrogen contents were adopted as stated in the original publications even if hydrogen contents on the same or a similar wadsleyite sample were later redetermined with a different technique (Jacobsen et al. 2005; Mao et al. 2008, 2011; Chang et al. 2015). This conservative approach retains the spread in estimated hydrogen contents resulting from the use of different methods and calibrations such as the unit cell axis ratio b/a as obtained by single-crystal X-ray diffraction (Jacobsen et al. 2005), or direct measurements by secondary ion mass spectrometry (SIMS), Fourier transform infrared absorption spectroscopy (FTIR) (Paterson 1982; Libowitzky and Rossman 1997; Deon et al. 2010), nuclear magnetic resonance (Kleppe et al. 2001), and neutron diffraction (Purevjav et al. 2016). When stated as H_2O wt%, we converted hydrogen contents to H_2O molecular equivalents per formula unit taking into account the iron content and molar mass of the respective wadsleyite sample. Hydrogen contents stated as H_2O wt% are strictly comparable only among samples with similar iron contents. For example, the hydrogen content for the hydrous wadsleyite sample ($Mg_{1.75}SiH_{0.5}O_4$) studied by Kudoh et al. (1996), Yusa and Inoue (1997), Kudoh and Inoue (1998), and Kudoh and Inoue (1999) of 2.5(3) wt% H_2O (Inoue et al. 1995; Yusa and Inoue 1997) translates to $y = 0.1894(187)$.

Unit cell volumes. End member unit cell volumes were obtained by fitting Equation 5 to the unit cell volumes listed in Appendix Table S5 and unit cell volumes for different spinelloid III compositions (Table 4 in Woodland and Angel 2000; Table 2 in Woodland et al. 2012). Unit cell volumes that deviate significantly from any compositional trend were excluded from the fit. Excluding, in addition, unit cell volumes for which the hydrogen concentration was estimated using the b/a axis ratio (Jacobsen et al. 2005), and hence not determined directly, changed only slightly the estimate of the unit cell volume for the MgH_2SiO_4 end member to $V_{hywa\ 0} = 546.3(24)$ $Å^3$ while leaving the other end member unit cell volumes unchanged. Excluding from the fit the

unit cell volume of the oxidized sample of Smyth et al. (1997) that falls slightly outside the quaternary system had no effect on the end member unit cell volumes.

Bulk and linear moduli. When reanalyzing volume and linear compression curves with second-order Birch-Murnaghan (BM-2) equations of state (EOS) (Equations 1 and 2), we treated unit cell volumes and unit cell edge lengths at ambient conditions as free parameters. We calculated Voigt and Reuss bounds on the bulk modulus using the linear moduli obtained from the reanalysis of experimental axial compression curves (Equation 3). All results are compiled in Appendix Table S6 together with references to the compression curves shown in Appendix Figure S7. This uniform analysis procedure removes differences in EOS parameters arising from different parametrization schemes.

In the case of studies using dynamic methods, we selected adiabatic elastic constants and moduli determined at ambient conditions, when available, as they should not be affected by the choice of the EOS. When the ambient conditions moduli were not listed or determined, we relied on the moduli as extracted from the EOS analysis without correcting for the EOS order. For the conversion of adiabatic elastic constants and moduli to isothermal quantities, we assumed the Grüneisen tensor to be isotropic $\gamma_i = \gamma$ ($i = 1, 2, 3$) (Stixrude and Lithgow-Bertelloni 2005, 2011) and calculated the isochoric heat capacity C_V using a Debye model as described in Ita and Stixrude (1992) and Stixrude and Lithgow-Bertelloni (2005) with Grüneisen parameters γ and other thermodynamic quantities given in Stixrude and Lithgow-Bertelloni (2011).

For Brillouin spectroscopy studies, we converted individual adiabatic elastic constants c_{ijS} to isothermal constants c_{ijT} by applying the relation $c_{ijT} = c_{ijS} - \gamma_i \gamma_j T C_V / V$ (Wehner and Klein 1971; Davies 1974). From the isothermal single-crystal elastic constants, we calculated isothermal linear moduli $k_i^R = 1/(s_{i1} + s_{i2} + s_{i3})$ in the Reuss bound and isothermal bulk moduli in both the Reuss and Voigt bound (Equation 3). Ultrasonic interferometry and resonant ultrasound

spectroscopy have been used to characterize the elasticity of wadsleyite polycrystals to directly determine aggregate bulk and shear moduli (e.g. Gwanmesia et al. 1990; Li et al. 1996; Katsura et al. 2001; Isaak et al. 2007). Since the stress states of individual grains during these measurements are unclear, polycrystal moduli cannot be easily related or converted to Voigt and Reuss bounds. Adiabatic bulk moduli were converted to isothermal bulk moduli using the relation $K_T = K_S - \gamma^2 T C_V / V$ with the same thermoelastic parameters and formulation as for single-crystal elastic constants (Stixrude and Lithgow-Bertelloni 2005, 2011). For the bulk modulus and typical wadsleyite compositions, this correction amounts to about 1.3 GPa.

References cited

Bolfan-Casanova, N., Muñoz, M., McCammon, C., Deloule, E., Férot, A., Demouchy, S., France, L., Andrault, D., and Pascarelli, S. (2012) Ferric iron and water incorporation in wadsleyite under hydrous and oxidizing conditions: A XANES, Mössbauer, and SIMS study. American Mineralogist, 97, 1483–1493.

Chang, Y.-Y., Jacobsen, S.D., Bina, C.R., Thomas, S.-M., Smyth, J.R., Frost, D.J., Boffa Ballaran, T., McCammon, C.A., Hauri, E.H., Inoue, T., and others (2015) Comparative compressibility of hydrous wadsleyite and ringwoodite: Effect of H_2O and implications for detecting water in the transition zone. Journal of Geophysical Research: Solid Earth, 120, 8259–8280.

Davies, G.F. (1974) Effective elastic moduli under hydrostatic stress—I. Quasi-harmonic theory. Journal of Physics and Chemistry of Solids, 35, 1513–1520.

Deon, F., Koch-Müller, M., Rhede, D., Gottschalk, M., Wirth, R., and Thomas, S.-M. (2010) Location and quantification of hydroxyl in wadsleyite: New insights. American Mineralogist, 95, 312–322.

Fei, Y., Mao, H., Shu, J., Parthasarathy, G., Bassett, W.A., and Ko, J. (1992) Simultaneous high-P, high-T X ray diffraction study of β-$(Mg,Fe)_2SiO_4$ to 26 GPa and 900 K. Journal of Geophysical Research: Solid Earth, 97, 4489–4495.

Finger, L.W., Hazen, R.M., Zhang, J., Ko, J., and Navrotsky, A. (1993) The effect of Fe on the crystal structure of wadsleyite β-$(Mg_{1-x}Fe_x)_2SiO_4$, $0.00 \leq x \leq 0.40$. Physics and Chemistry of Minerals, 19, 361–368.

Fujisawa, H. (1998) Elastic wave velocities of forsterite and its β-spinel form and chemical boundary hypothesis for the 410-km discontinuity. Journal of Geophysical Research: Solid Earth, 103, 9591–9608.

Griffin, J.M., Berry, A.J., Frost, D.J., Wimperis, S., and Ashbrook, S.E. (2013) Water in the Earth's mantle: a solid-state NMR study of hydrous wadsleyite. Chemical Science, 4, 1523–1538.

Gwanmesia, G.D., Liebermann, R.C., and Guyot, F. (1990) Hot-pressing and characterization of polycrystals of β-Mg_2SiO_4, for acoustic velocity measurements. Geophysical Research Letters, 17, 1331–1334.

Hazen, R.M., Zhang, J., and Ko, J. (1990) Effects of Fe/Mg on the compressibility of synthetic wadsleyite: β-$(Mg_{1-x}Fe_x)_2SiO_4$ $(x \leq 0.25)$. Physics and Chemistry of Minerals, 17, 416–419.

Hazen, R.M., Weinberger, M.B., Yang, H., and Prewitt, C.T. (2000a) Comparative high-pressure crystal chemistry of wadsleyite, β-$(Mg_{1-x}Fe_x)_2SiO_4$, with $x = 0$ and 0.25. American Mineralogist, 85, 770–777.

Hazen, R.M., Yang, H., and Prewitt, C.T. (2000b) High-pressure crystal chemistry of Fe^{3+}-wadsleyite, β-$Fe_{2.33}Si_{0.67}O_4$. American Mineralogist, 85, 778–783.

Holl, C.M., Smyth, J.R., Jacobsen, S.D., and Frost, D.J. (2008) Effects of hydration on the structure and compressibility of wadsleyite, β-(Mg_2SiO_4). American Mineralogist, 93, 598–607.

Horiuchi, H., and Sawamoto, H. (1981) β-Mg_2SiO_4: Single-crystal X-ray diffraction study. American Mineralogist, 66, 568–575.

Inoue, T., Yurimoto, H., and Kudoh, Y. (1995) Hydrous modified spinel, $Mg_{1.75}SiH_{0.5}O_4$: A new water reservoir in the mantle transition region. Geophysical Research Letters, 22, 117–120.

Inoue, T., Tanimoto, Y., Irifune, T., Suzuki, T., Fukui, H., and Ohtaka, O. (2004) Thermal expansion of wadsleyite, ringwoodite, hydrous wadsleyite and hydrous ringwoodite. Physics of the Earth and Planetary Interiors, 143–144, 279–290.

Isaak, D.G., Gwanmesia, G.D., Falde, D., Davis, M.G., Triplett, R.S., and Wang, L. (2007) The elastic properties of β-Mg_2SiO_4 from 295 to 660 K and implications on the composition of Earth's upper mantle. Physics of the Earth and Planetary Interiors, 162, 22–31.

Isaak, D.G., Gwanmesia, G.D., Davis, M.G., Stafford, S.C., Stafford, A.M., and Triplett, R.S. (2010) The temperature dependence of the elasticity of Fe-bearing wadsleyite. Physics of the Earth and Planetary Interiors, 182, 107–112.

Ita, J., and Stixrude, L. (1992) Petrology, elasticity, and composition of the mantle transition zone. Journal of Geophysical Research: Solid Earth, 97, 6849–6866.

Jacobsen, S.D., Demouchy, S., Frost, D.J., Ballaran, T.B., and Kung, J. (2005) A systematic study of OH in hydrous wadsleyite from polarized FTIR spectroscopy and single-crystal X-ray diffraction: Oxygen sites for hydrogen storage in Earth's interior. American Mineralogist, 90, 61–70.

Katsura, T., Mayama, N., Shouno, K., Sakai, M., Yoneda, A., and Suzuki, I. (2001) Temperature derivatives of elastic moduli of $(Mg_{0.91}Fe_{0.09})_2SiO_4$ modified spinel. Physics of the Earth and Planetary Interiors, 124, 163–166.

Kawazoe, T., Chaudhari, A., Smyth, J.R., and McCammon, C. (2016) Coupled substitution of Fe^{3+} and H^+ for Si in wadsleyite: A study by polarized infrared and Mössbauer spectroscopies and single-crystal X-ray diffraction. American Mineralogist, 101, 1236–1239.

Kleppe, A.K., Jephcoat, A.P., Olijnyk, H., Slesinger, A.E., Kohn, S.C., and Wood, B.J. (2001) Raman spectroscopic study of hydrous wadsleyite (β-Mg_2SiO_4) to 50 GPa. Physics and Chemistry of Minerals, 28, 232–241.

Kohlstedt, D.L., Keppler, H., and Rubie, D.C. (1996) Solubility of water in the α, β and γ phases of $(Mg,Fe)_2SiO_4$. Contributions to Mineralogy and Petrology, 123, 345–357.

Kudoh, Y., and Inoue, T. (1998) Effect of pressure on the crystal structure of hydrous wadsleyite, $Mg_{1.75}SiH_{0.5}O_4$. In M.H. Manghnani and T. Yagi, Eds., Properties of Earth and Planetary Materials at High Pressure and Temperature pp. 517–521. American Geophysical Union, Washington, DC.

Kudoh, Y., and Inoue, T. (1999) Mg-vacant structural modules and dilution of the symmetry of hydrous wadsleyite, β-$Mg_{2-x}SiH_{2x}O_4$ with $0.00 \leq x \leq 0.25$. Physics and Chemistry of Minerals, 26, 382–388.

Kudoh, Y., Inoue, T., and Arashi, H. (1996) Structure and crystal chemistry of hydrous wadsleyite, $Mg_{1.75}SiH_{0.5}O_4$: possible hydrous magnesium silicate in the mantle transition zone. Physics and Chemistry of Minerals, 23, 461–469.

Li, B., and Liebermann, R.C. (2000) Sound velocities of wadsleyite β-$(Mg_{0.88}Fe_{0.12})_2SiO_4$ to 10 GPa. American Mineralogist, 85, 292–295.

Li, B., Gwanmesia, G.D., and Liebermann, R.C. (1996) Sound velocities of olivine and beta polymorphs of Mg_2SiO_4 at Earth's transition zone pressures. Geophysical Research Letters, 23, 2259–2262.

Li, B., Liebermann, R.C., and Weidner, D.J. (1998) Elastic moduli of wadsleyite (β-Mg_2SiO_4) to 7 gigapascals and 873 Kelvin. Science, 281, 675–677.

——— (2001) P-V-V_p-V_s-T measurements on wadsleyite to 7 GPa and 873 K: Implications for the 410-km seismic discontinuity. Journal of Geophysical Research: Solid Earth, 106, 30579–30591.

Libowitzky, E., and Rossman, G.R. (1996) Principles of quantitative absorbance measurements in anisotropic crystals. Physics and Chemistry of Minerals, 23, 319–327.

——— (1997) An IR absorption calibration for water in minerals. American Mineralogist, 82, 1111–1115.

Liu, W., Kung, J., Li, B., Nishiyama, N., and Wang, Y. (2009) Elasticity of $(Mg_{0.87}Fe_{0.13})_2SiO_4$ wadsleyite to 12 GPa and 1073 K. Physics of the Earth and Planetary Interiors, 174, 98–104.

Mao, Z., Jacobsen, S.D., Jiang, F., Smyth, J.R., Holl, C.M., and Duffy, T.S. (2008a) Elasticity of hydrous wadsleyite to 12 GPa: Implications for Earth's transition zone. Geophysical Research Letters, 35, L21305.

Mao, Z., Jacobsen, S.D., Jiang, F.M., Smyth, J.R., Holl, C.M., Frost, D.J., and Duffy, T.S. (2008b) Single-crystal elasticity of wadsleyites, β-Mg_2SiO_4, containing 0.37–1.66 wt.% H_2O. Earth and Planetary Science Letters, 268, 540–549.

Mao, Z., Jacobsen, S.D., Frost, D.J., McCammon, C.A., Hauri, E.H., and Duffy, T.S. (2011) Effect of hydration on the single-crystal elasticity of Fe-bearing wadsleyite to 12 GPa. American Mineralogist, 96, 1606–1612.

Mayama, N., Suzuki, I., Saito, T., Ohno, I., Katsura, T., and Yoneda, A. (2004) Temperature dependence of elastic moduli of β-$(Mg, Fe)_2SiO_4$. Geophysical Research Letters, 31, L04612.

McCammon, C.A., Frost, D.J., Smyth, J.R., Laustsen, H.M.S., Kawamoto, T., Ross, N.L., and van Aken, P.A. (2004) Oxidation state of iron in hydrous mantle phases: implications for

subduction and mantle oxygen fugacity. Physics of the Earth and Planetary Interiors, 143–144, 157–169.

Mizukami, S., Ohtani, A., Kawai, N., and Ito, E. (1975) High-pressure X-ray diffraction studies on β- and γ-Mg$_2$SiO$_4$. Physics of the Earth and Planetary Interiors, 10, 177–182.

Mrosko, M., Koch-Müller, M., McCammon, C., Rhede, D., Smyth, J.R., and Wirth, R. (2015) Water, iron, redox environment: effects on the wadsleyite–ringwoodite phase transition. Contributions to Mineralogy and Petrology, 170, 9.

Paterson, M.S. (1982) The determination of hydroxyl by infrared absorption in quartz, silicate glasses and similar materials. Bulletin de Minéralogie, 105, 20–29.

Prescher, C., McCammon, C., and Dubrovinsky, L. (2012) *MossA*: a program for analyzing energy-domain Mössbauer spectra from conventional and synchrotron sources. Journal of Applied Crystallography, 45, 329–331.

Purevjav, N., Okuchi, T., Tomioka, N., Wang, X., and Hoffmann, C. (2016) Quantitative analysis of hydrogen sites and occupancy in deep mantle hydrous wadsleyite using single crystal neutron diffraction. Scientific Reports, 6, 34988.

Sano-Furukawa, A., Kuribayashi, T., Komatsu, K., Yagi, T., and Ohtani, E. (2011) Investigation of hydrogen sites of wadsleyite: A neutron diffraction study. Physics of the Earth and Planetary Interiors, 189, 56–62.

Sawamoto, H. (1986) Single crystal growth of the modified spinel (β) and spinel (γ) phases of (Mg,Fe)$_2$SiO$_4$ and some geophysical implications. Physics and Chemistry of Minerals, 13, 1–10.

Sawamoto, H., Weidner, D.J., Sasaki, S., and Kumazawa, M. (1984) Single-crystal elastic properties of the modified spinel (beta) phase of magnesium orthosilicate. Science, 224, 749–751.

Sinogeikin, S.V., Katsura, T., and Bass, J.D. (1998) Sound velocities and elastic properties of Fe-bearing wadsleyite and ringwoodite. Journal of Geophysical Research: Solid Earth, 103, 20819–20825.

Smyth, J.R., Kawamoto, T., Jacobsen, S.D., Swope, R.J., Hervig, R.L., and Holloway, J.R. (1997) Crystal structure of monoclinic hydrous wadsleyite [β-$(Mg,Fe)_2SiO_4$]. American Mineralogist, 82, 270–275.

Smyth, J.R., Bolfan-Casanova, N., Avignant, D., El-Ghozzi, M., and Hirner, S.M. (2014) Tetrahedral ferric iron in oxidized hydrous wadsleyite. American Mineralogist, 99, 458–466.

Stixrude, L., and Lithgow-Bertelloni, C. (2005) Thermodynamics of mantle minerals — I. Physical properties. Geophysical Journal International, 162, 610–632.

——— (2011) Thermodynamics of mantle minerals — II. Phase equilibria. Geophysical Journal International, 184, 1180–1213.

Suzuki, I., Ohtani, E., and Kumazawa, M. (1980) Thermal expansion of modified spinel, β-Mg_2SiO_4. Journal of Physics of the Earth, 28, 273–280.

Trots, D.M., Kurnosov, A., Ballaran, T.B., and Frost, D.J. (2012) High-temperature structural behaviors of anhydrous wadsleyite and forsterite. American Mineralogist, 97, 1582–1590.

Wang, J., Bass, J.D., and Kastura, T. (2014) Elastic properties of iron-bearing wadsleyite to 17.7 GPa: Implications for mantle mineral models. Physics of the Earth and Planetary Interiors, 228, 92–96.

Wehner, R.K., and Klein, R. (1971) Adiabatic and isothermal elastic constants from space- and time-dependent response theory. Physica, 52, 92–108.

Woodland, A.B., and Angel, R.J. (1998) Crystal structure of a new spinelloid with the wadsleyite structure in the system Fe_2SiO_4-Fe_3O_4 and implications for the Earth's mantle. American Mineralogist, 83, 404–408.

——— (2000) Phase relations in the system fayalite–magnetite at high pressures and temperatures. Contributions to Mineralogy and Petrology, 139, 734–747.

Woodland, A.B., Angel, R.J., and Koch, M. (2012) Structural systematics of spinel and spinelloid phases in the system MFe_2O_4–M_2SiO_4 with $M = Fe^{2+}$ and Mg. European Journal of Mineralogy, 24, 657–668.

Ye, Y., Schwering, R.A., and Smyth, J.R. (2009) Effects of hydration on thermal expansion of forsterite, wadsleyite, and ringwoodite at ambient pressure. American Mineralogist, 94, 899–904.

Ye, Y., Smyth, J.R., Hushur, A., Manghnani, M.H., Lonappan, D., Dera, P., and Frost, D.J. (2010) Crystal structure of hydrous wadsleyite with 2.8% H_2O and compressibility to 60 GPa. American Mineralogist, 95, 1765–1772.

Yusa, H., and Inoue, T. (1997) Compressibility of hydrous wadsleyite (β-phase) in Mg_2SiO_4 by high pressure X-ray diffraction. Geophysical Research Letters, 24, 1831–1834.

Zha, C., Duffy, T.S., Mao, H., Downs, R.T., Hemley, R.J., and Weidner, D.J. (1997) Single-crystal elasticity of β-Mg_2SiO_4 to the pressure of the 410 km seismic discontinuity in the Earth's mantle. Earth and Planetary Science Letters, 147, E9–E15.

Appendix Figures

Figure S1
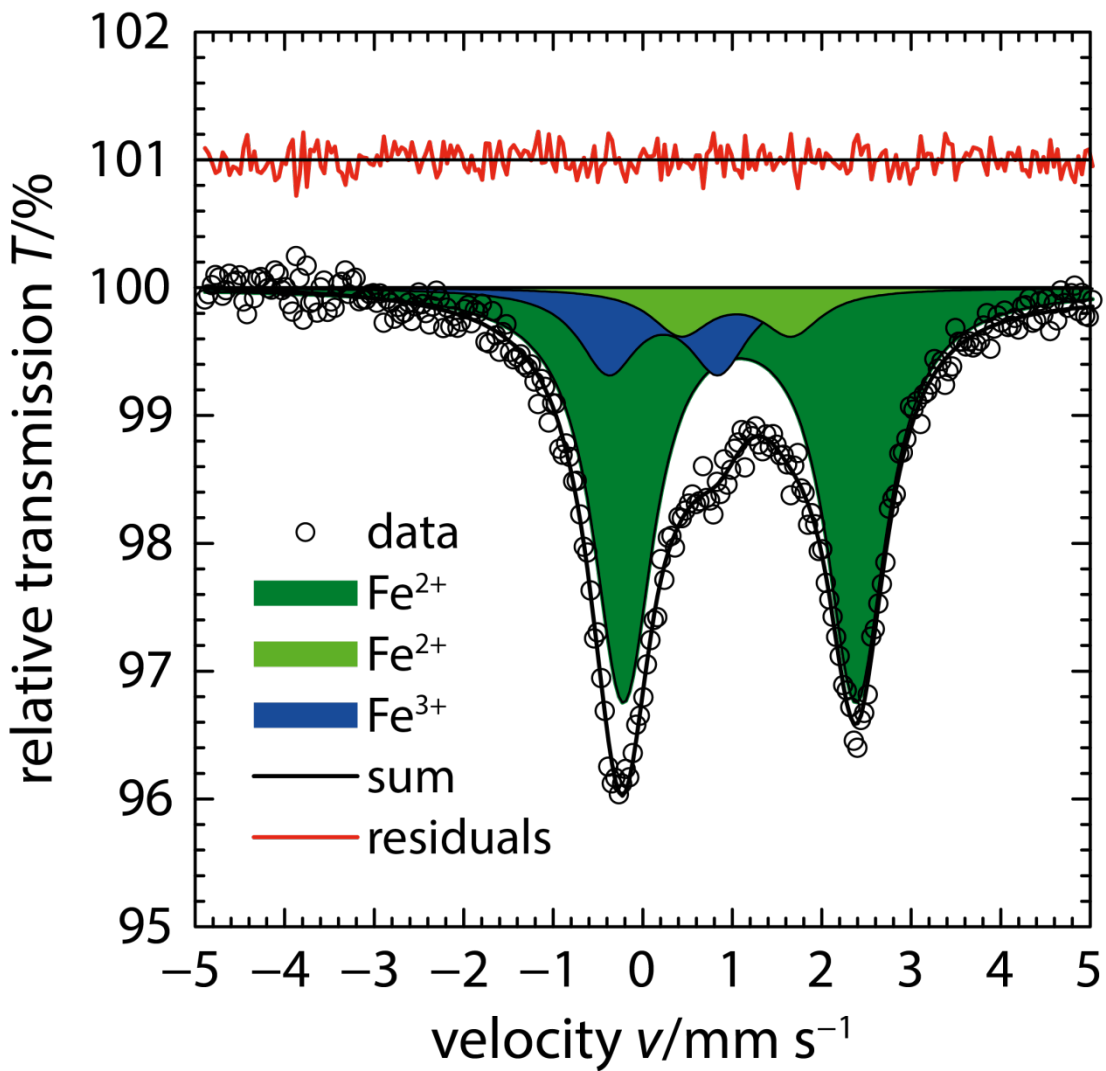
Appendix Figure S1. Mössbauer spectrum of wadsleyite powder. The deconvolution according to model 4 (Appendix Table S2) includes two doublets for Fe^{2+} and one doublet for Fe^{3+}. The extra Fe^{2+} doublet may arise from variations in the next-nearest neighbor environment of Fe^{2+} due to solid solution effects.

Figure S2
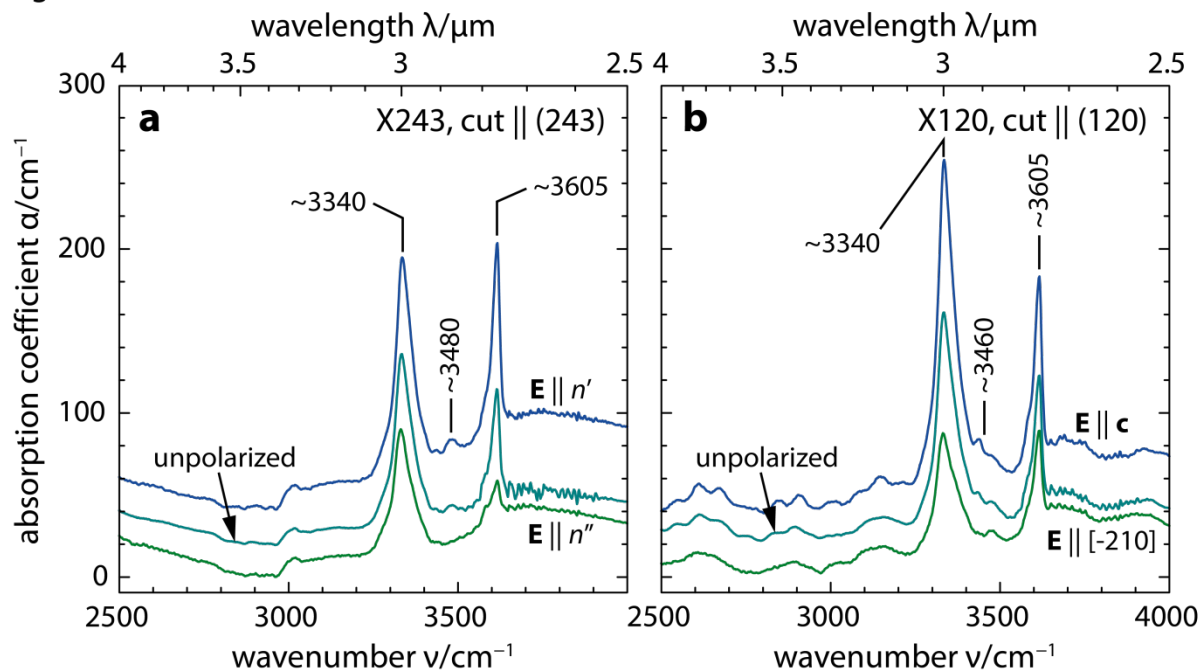
Appendix Figure S2. Polarized and unpolarized FTIR absorption spectra for the crystal sections cut parallel to the (**a**) (243) and (**b**) (120) plane. The prominent absorption bands around 3340 cm^{-1} and 3600 cm^{-1} arise from structurally bonded hydroxyl groups in wadsleyite. Both bands show pleochroism. Note also the weak absorption feature around 3500 cm^{-1}. (Spectra vertically offset for clarity).

Figure S3
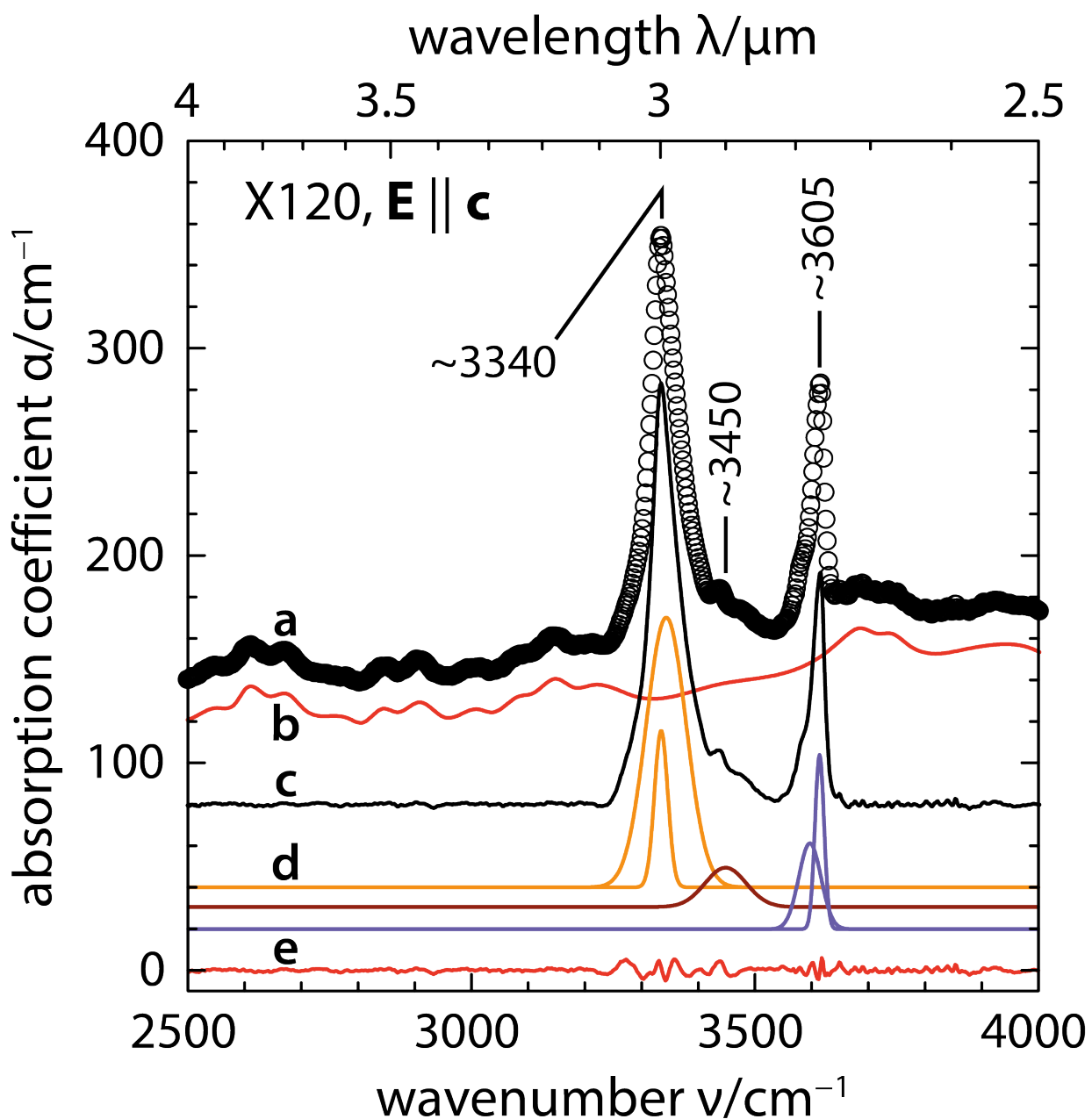
Appendix Figure S3. Background correction and deconvolution for the spectrum with **E ∥ c** recorded on the section cut parallel to (120). (**a**) Raw spectrum, (**b**) background, (**c**) background-corrected spectrum, (**d**) individual peaks grouped to bands at 3340 cm^{-1}, 3450 cm^{-1}, and 3605 cm^{-1}, (**e**) residual absorption. (Components vertically offset for clarity).

Figure S4
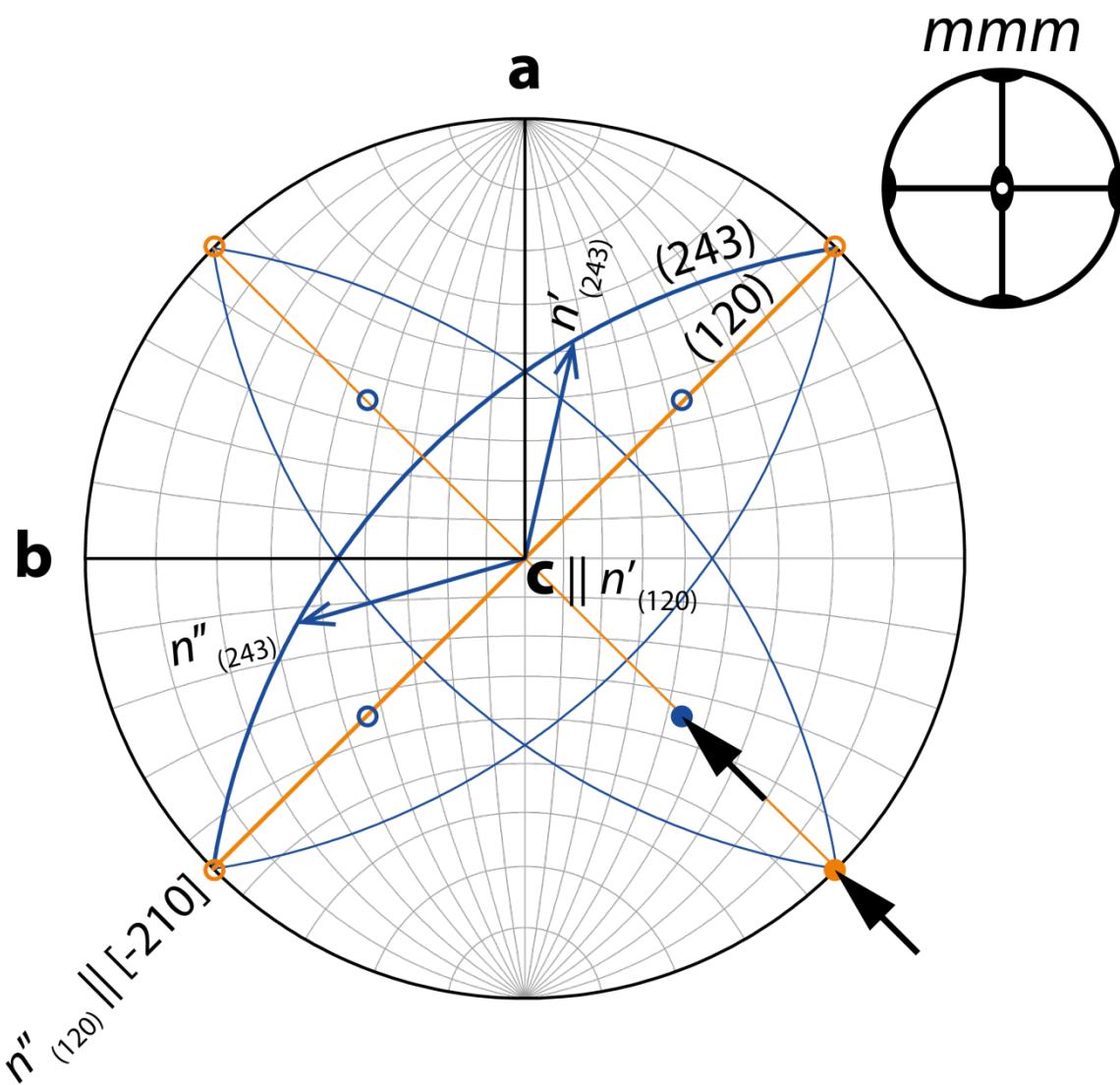
Appendix Figure S4. Stereographic projection (lower hemisphere) illustrating the orientation relationships between the two crystal sections (thick lines; poles: solid circles), their optical vibration directions (*n'* and *n''*), and the compression direction of the diamond anvil cell (black arrows). For each section, the symmetry equivalents {243} and {120} are shown (thin lines; poles: open circles).

Figure S5
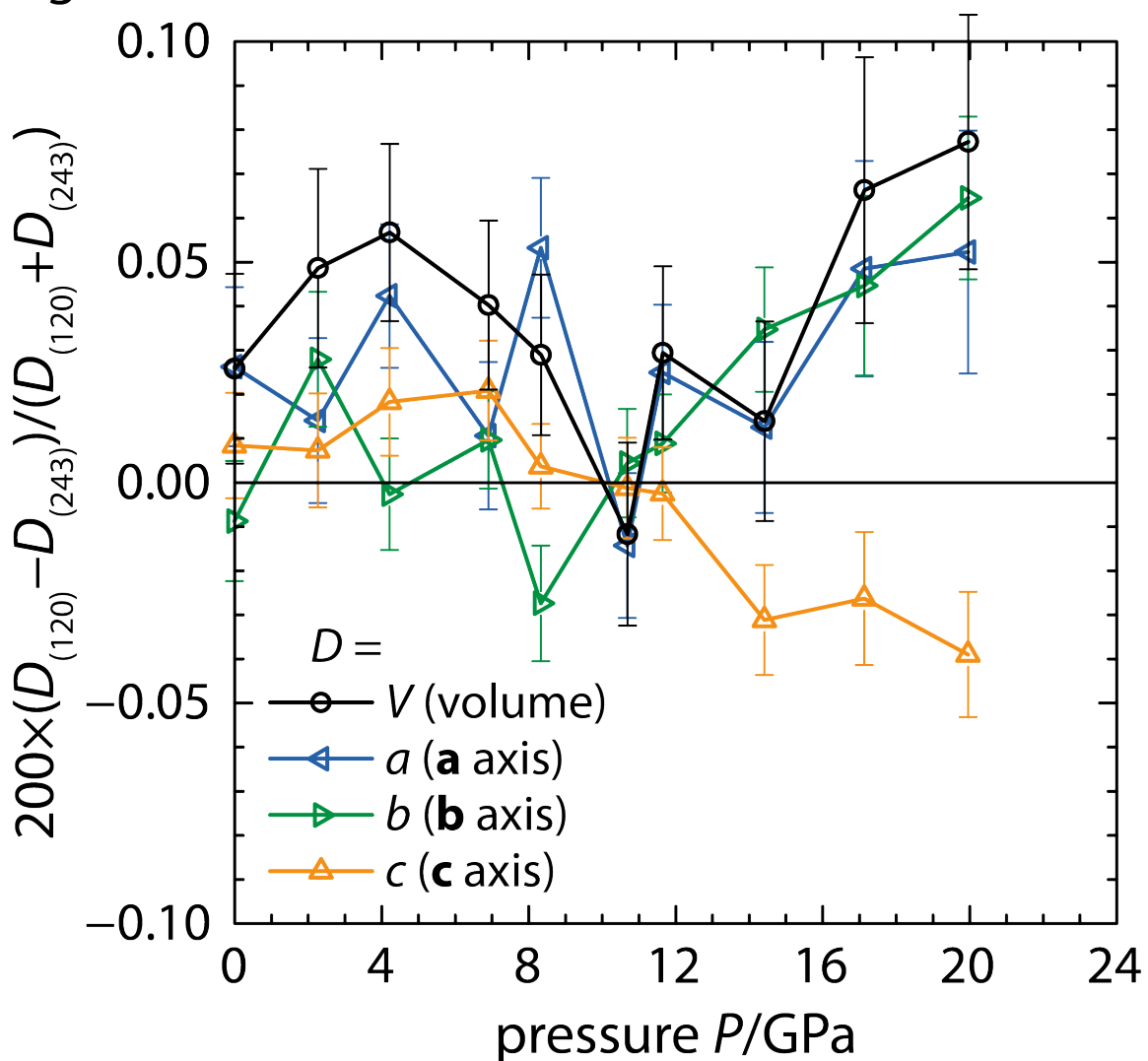
Appendix Figure S5. Relative differences in volume and unit cell edge lengths between the two crystals as a function of pressure. Note the diverging trends for pressures above 12 GPa that might point to the presence of deviatoric stresses.

Figure S6
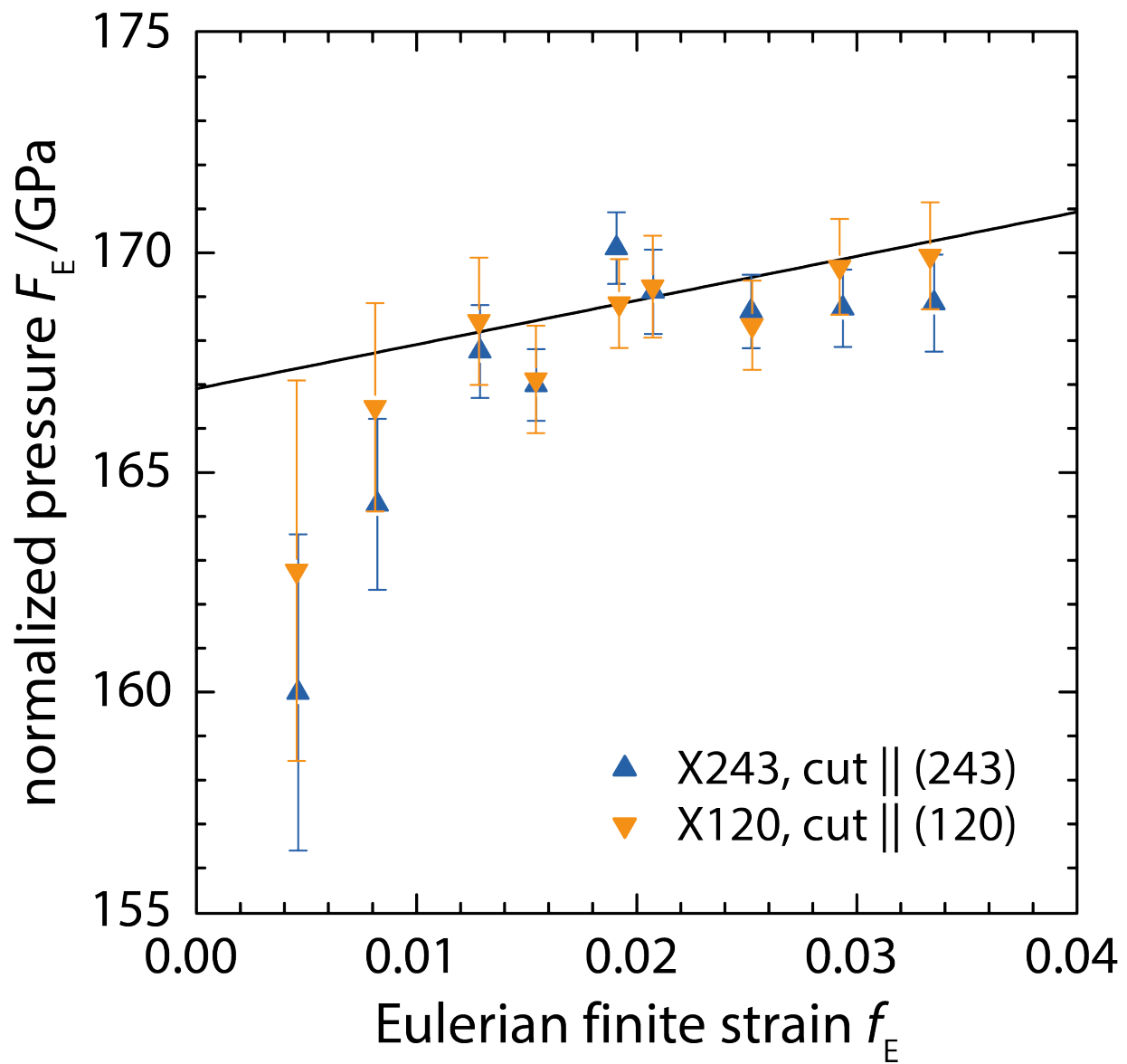
Appendix Figure S6. Normalized pressure as a function of Eulerian finite strain (*F-f* plot). The

black line was drawn according to the combined third-order Birch-Murnaghan EOS (Table 2).

Figure S7
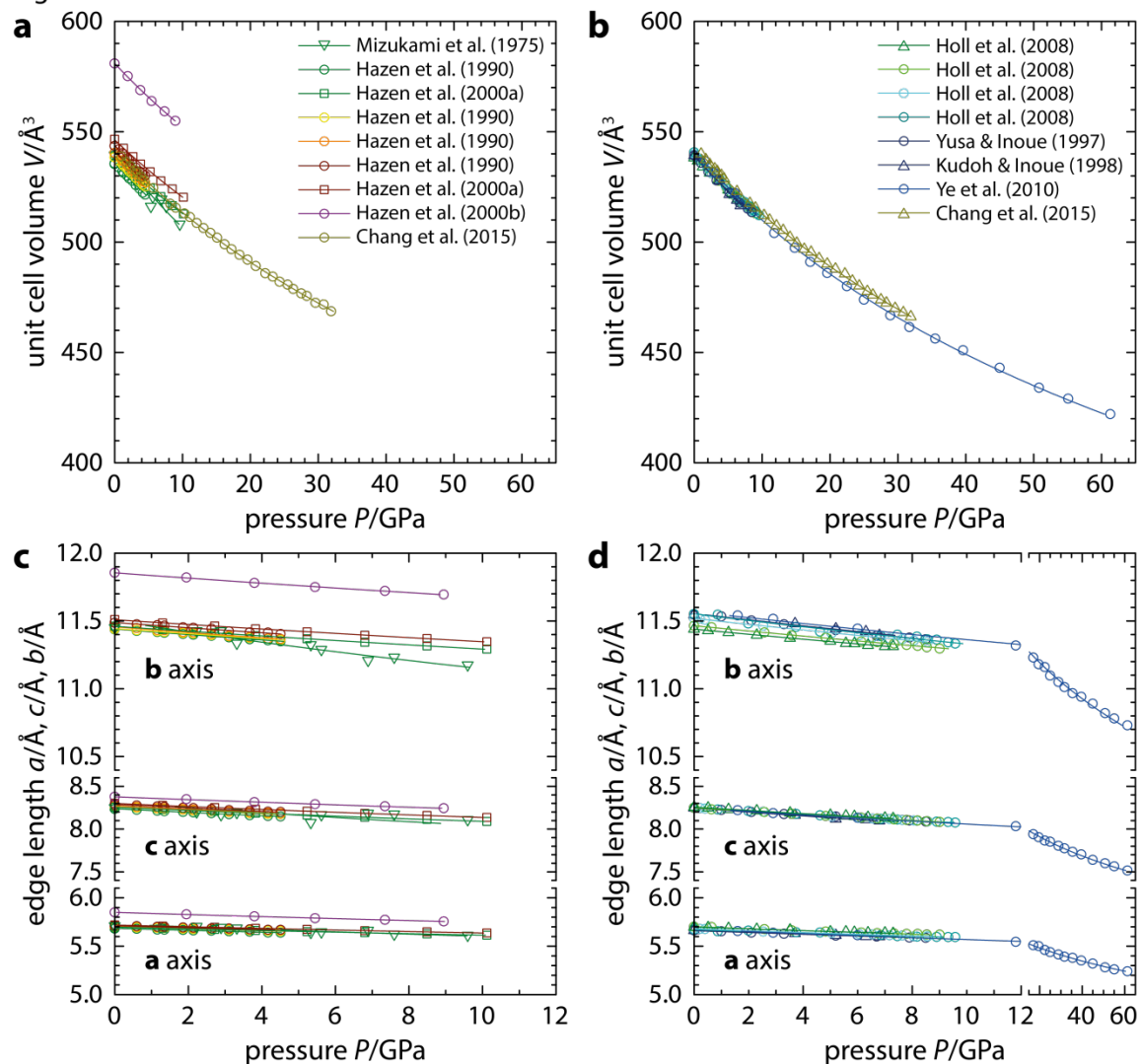
Appendix Figure S7. (a,b) Volume and **(c,d)** linear compression curves for **(a,c)** iron-bearing and **(b,d)** hydrous wadsleyites. See Appendix Table S6 for references and compositions. Lines show second-order Birch-Murnaghan EOS curves.

Figure S8
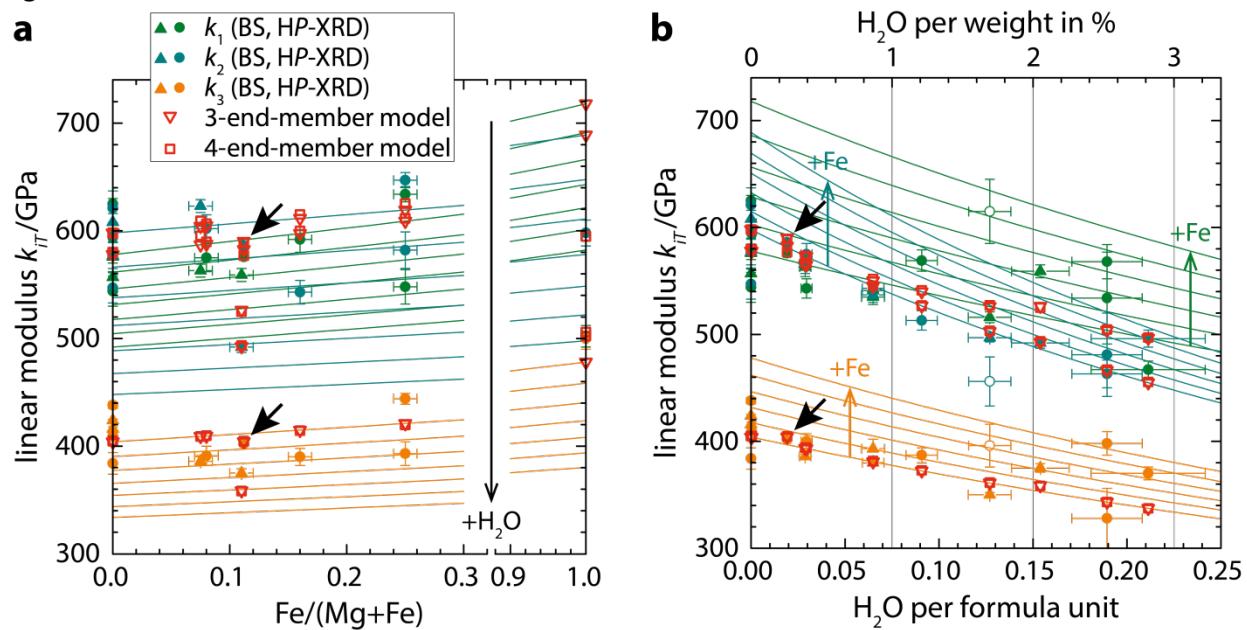
Appendix Figure S8. Isothermal linear moduli for wadsleyite as a function of (**a**) Fe/(Mg+Fe) and (**b**) H_2O molecular equivalents per formula unit. See Appendix Table S6 for references. Contours were calculated from the 3-end member model (Table 3) and range from 0 wt% H_2O to 3 wt% H_2O in steps of 0.5 wt% H_2O in (**a**) and from Fe/(Mg+Fe) = 0 to 1 in steps of 0.2 in (**b**). In (**a**), compositions spread vertically for different hydrogen and ferric iron contents. In (**b**), compositions spread vertically for different iron (ferrous and ferric) contents. Solid arrows indicate the composition of the present study. Data points with open symbols were not included in the multi-end member analysis. HP-XRD high-pressure X-ray diffraction, BS Brillouin spectroscopy.

Appendix Tables

Appendix Table S1. Electron microprobe analysis

Oxide	wt%	Atoms per 4 oxygens	
SiO_2	41.3(2)	Si	1.020(6)
Al_2O_3	0.03(1)	Al	0.0009(3)
FeO	10.6(2)	Fe	0.219(4)
MnO	0.13(3)	Mn	0.0027(6)
MgO	47.0(3)	Mg	1.73(1)
CaO	0.007(6)	Ca	0.0002(2)
NiO	0.37(4)	Ni	0.0073(8)
Total	99.4(4)	Total	2.98(2)
		Fe/(Mg+Fe)	0.112(2)
		M^a/Si	1.92(1)

[a] M = Al+Fe+Mn+Mg+Ca+Ni.

Appendix Table S2.

Hyperfine parameters from room temperature Mössbauer spectrum

$\chi^2 = 1.14$	CS^a (mm s^{-1})	QS^b (mm s^{-1})	$FWHM^c$ (mm s^{-1})	A^d (%)
Doublet 1: Fe^{2+}	1.08(1)	2.60(3)	0.80(4)	77(3)
Doublet 2: Fe^{2+}	1.04(10)	1.2(2)	0.80(4)	8(2)
Doublet 3: Fe^{3+}	0.23(6)	1.23(13)	0.8(2)	15(3)

[a] Center shift relative to α-Fe.

[b] Quadrupole splitting.

[c] Full width at half maximum.

[d] Area fraction.

Appendix Table S3. Infrared absorption band parameters and hydrogen concentrations

Crystal	X120, cut || (120)			X243, cut || (243)		
Spectrum	unpolarized	$E \parallel c$	$E \parallel [-210]$	unpolarized	$E \parallel n'$	$E \parallel n''$
3100 - 3455 cm^{-1}						
$\langle\nu\rangle$ (cm^{-1})	3343.1(3)	3341.9(2)	3344.1(4)	3338.5(2)	3341.3(2)	3336.2(2)
A_{INT} (cm^{-2})	10162(70)	13694(89)	6199(53)	6938(86)	9155(109)	5504(52)
H$_2$O^a (mol L^{-1})	0.30(6)	0.14(3)	0.06(1)	0.20(4)	0.09(2)	0.05(1)
H$_2$O^b (mol L^{-1})	0.25(13)	0.11(4)	0.05(4)	0.16(24)	0.07(4)	0.04(4)
H$_2$O^c (mol L^{-1})	0.42(4)	0.19(2)	0.08(1)	0.29(3)	0.13(1)	0.08(1)
3455 - 3515 cm^{-1}						
$\langle\nu\rangle$ (cm^{-1})	3458(1)	3449(1)	3470(1)	3484(2)	3481(1)	–
A_{INT} (cm^{-2})	1266(46)	1725(63)	714(28)	211(20)	731(27)	–
H$_2$O^a (mol L^{-1})	0.05(1)	0.023(5)	0.010(2)	0.010(2)	0.011(2)	–
H$_2$O^b (mol L^{-1})	0.02(4)	0.007(8)	0.01(1)	0.01(9)	0.01(1)	–
H$_2$O^c (mol L^{-1})	0.05(1)	0.024(2)	0.010(1)	0.009(1)	0.010(1)	–
3515 - 3700 cm^{-1}						
$\langle\nu\rangle$ (cm^{-1})	3604.7(6)	3605.0(4)	3605.0(5)	3604.5(5)	3605.4(3)	3601(1)
A_{INT} (cm^{-2})	2569(83)	3722(78)	1968(53)	2425(60)	3873(62)	948(45)
H$_2$O^a (mol L^{-1})	0.21(4)	0.10(2)	0.05(1)	0.20(4)	0.11(2)	0.025(5)
H$_2$O^b (mol L^{-1})	0.15(22)	0.07(5)	0.04(8)	0.14(52)	0.08(6)	0.02(8)
H$_2$O^c (mol L^{-1})	0.11(1)	0.051(5)	0.027(3)	0.10(1)	0.053(5)	0.013(1)
Total						
$A \parallel [-210]$ (cm^{-2})		8882(80)			9848(70)	
$A \parallel c$ (cm^{-2})		19141(134)			10364(76)	
A_{TOT} (cm^{-2})		36905(208)			30060(159)	
H$_2$O^a (wt%)	0.28(4)	0.26(2)		0.21(3)	0.22(2)	
H$_2$O^b (wt%)	0.21(13)	0.19(10)		0.15(29)	0.16(8)	
H$_2$O^c (wt%)	0.29(3)	0.25(2)		0.20(2)	0.21(1)	

[a] Calibration of Libowitzky and Rossman (1997).

[b] Calibration of Paterson (1982).

[c] Calibration of Deon et al. (2010).

Appendix Table S4. Unit cell edge lengths and volumes at high pressures

Pressure	X120, cut ‖ (120)				X243, cut ‖ (243)			
P (GPa)	a (Å)	b (Å)	c (Å)	V (Å^3)	a (Å)	b (Å)	c (Å)	V (Å^3)
0.00(3)	5.7087(9)	11.4760(14)	8.2770(7)	542.25(10)	5.7072(5)	11.4770(7)	8.2763(7)	542.11(6)
2.27(4)	5.6858(8)	11.4329(15)	8.2292(7)	534.94(9)	5.6850(7)	11.4297(9)	8.2286(8)	534.68(8)
4.22(4)	5.6691(7)	11.3958(12)	8.1932(6)	529.31(8)	5.6667(6)	11.3961(8)	8.1917(8)	529.01(7)
6.91(4)	5.6448(8)	11.3512(11)	8.1470(6)	522.02(8)	5.6442(5)	11.3501(6)	8.1453(7)	521.81(6)
8.34(4)	5.6335(8)	11.3226(14)	8.1225(6)	518.10(8)	5.6305(4)	11.3257(5)	8.1222(5)	517.95(5)
10.69(4)	5.6128(7)	11.2889(12)	8.0875(6)	512.44(8)	5.6136(6)	11.2884(7)	8.0876(7)	512.50(7)
11.65(6)	5.6065(7)	11.2733(11)	8.0722(6)	510.19(8)	5.6051(5)	11.2723(6)	8.0724(6)	510.04(6)
14.42(6)	5.5837(9)	11.2325(13)	8.0300(6)	503.63(9)	5.5830(6)	11.2286(9)	8.0325(8)	503.56(7)
17.14(8)	5.5643(11)	11.1960(20)	7.9934(9)	497.97(12)	5.5616(8)	11.1910(11)	7.9955(8)	497.64(9)
19.96(12)	5.5450(13)	11.1572(16)	7.9563(8)	492.23(11)	5.5421(8)	11.1500(13)	7.9594(8)	491.85(9)

Appendix Table S5. Unit cell parameters for wadsleyites of different compositions

Fe/(Mg+Fe)	H$_2$O (pfu)	Fe^{3+}/∑Fe	Unit cell edge lengths			Volume	Angle[a]	Sample[b]	Methods[c]	Reference
x	y	z	a (Å)	b (Å)	c (Å)	V (Å^3)	β (°)			
0		0	5.702(2)	11.440(6)	8.250(3)	538.2(4)		P	XRD	Suzuki et al. (1980)
0		0	5.6983(4)	11.4380(7)	8.2566(8)	538.14(7)		SX	XRD	Horiuchi and Sawamoto (1981)
0		0	5.696(1)	11.453(1)	8.256(1)	538.59(12)		SX	XRD EMPA	Sawamoto (1986)
0		0	5.6921(2)	11.460(1)	8.253(2)	538.3(2)		SX	XRD EMPA	Finger et al. (1993)
0	0	0	5.703(5)	11.424(4)	8.260(4)	538.1(9)		P	XRD	Inoue et al. (2004)
0	0	0	5.7007(5)	11.4456(10)	8.2580(13)	538.81(7)		SX	XRD	Ye et al. (2009)
0	0	0	5.70158(8)	11.44275(16)	8.24913(12)	538.188(13)		P	XRD	Trots et al. (2012)
0.075(10)			5.705(2)	11.450(4)	8.258(3)	539.4(4)		SX	XRD EMPA	Sinogeikin et al. (1998)
0.08(1)		0.08(2)[d]	5.7037(9)	11.4529(8)	8.2679(9)	540.1(1)		SX	XRD EMPA MS[d]	Finger et al. (1993)
0.10(1)			5.7107(5)	11.4675(9)	8.2778(10)	542.09(9)		SX	XRD EMPA	Sawamoto (1986)
0.16(1)		0.08(2)[d]	5.7119(9)	11.4681(8)	8.2799(9)	542.4(1)		SX	XRD EMPA MS[d]	Finger et al. (1993)
0.25(1)		0.08(2)[d]	5.717(1)	11.506(1)	8.299(1)	545.9(2)		SX	XRD EMPA MS[d]	Finger et al. (1993)
0.30(1)			5.7216(2)	11.4823(5)	8.2897(9)	544.61(7)		SX	XRD EMPA	Sawamoto (1986) *
0.395(9)		0	5.739(2)	11.515(2)	8.316(1)	549.6(2)		SX	XRD EMPA MS	Finger et al. (1993)
1		0.37(1)	5.8559(2)	11.8936(4)	8.3684(2)	582.84(2)		P	XRD EMPA	Woodland and Angel (1998)
0	0.0004(1)	0	5.7002(2)	11.4385(2)	8.2587(2)	538.46(2)	90.004(2)	SX	XRD FTIR	Jacobsen et al. (2005)
0	0.0004(1)	0	5.7008(5)	11.4407(12)	8.2582(7)	538.61(7)	90.000(9)	SX	XRD	Holl et al. (2008)
0	0.0012(1)	0	5.6998(2)	11.4383(3)	8.2573(2)	538.34(3)	90.003(2)	SX	XRD FTIR	Jacobsen et al. (2005)
0	0.0249(24)	0	5.6941(2)	11.4597(3)	8.2556(2)	538.70(3)	90.002(3)	SX	XRD FTIR	Jacobsen et al. (2005)
0	0.0295(29)	0	5.6951(3)	11.4628(7)	8.2565(9)	538.99(6)	90.001(9)	SX	XRD	Holl et al. (2008)
0	0.0465(44)	0	5.6881(3)	11.4868(3)	8.2508(2)	539.08(3)	90.055(3)	SX	XRD FTIR	Jacobsen et al. (2005)
0	0.0619(73)	0	5.693(6)	11.499(1)	8.258(9)	540.65(5)		SX	XRD SIMS	Deon et al. (2010)
0	0.0649(58)	0	5.6888(6)	11.4830(8)	8.2523(6)	539.08(8)		SX	XRD	Mao et al. (2008)
0	0.0741(69)	0	5.6890(4)	11.4830(4)	8.2527(4)	539.13(4)	90.085(4)	SX	XRD FTIR	Jacobsen et al. (2005)
0	0.0817(75)	0	5.6900(2)	11.4778(3)	8.2529(3)	538.98(3)	90.125(3)	SX	XRD FTIR	Jacobsen et al. (2005)
0	0.0908(83)	0	5.6862(4)	11.5023(13)	8.2526(6)	539.75(6)	90.013(9)	SX	XRD	Holl et al. (2008)
0	0.1050(20)	0	5.6865(4)	11.515(2)	8.2545(7)	540.52(5)	89.985(13)	P SX	XRD ND	Purevjav et al. (2016)
0	0.1113(123)	0	5.683(2)	11.514(2)	8.247(2)	539.7(2)		SX	XRD EMPA	Sano-Furukawa et al. (2011)
0	0.1225(68)	0	5.690(1)	11.628(6)	8.188(15)	541.80(8)		SX	XRD SIMS	Deon et al. (2010)
0	0.1263(111)	0	5.679(2)	11.548(2)	8.250(3)	541.1(4)		P	XRD EMPA NMR	Kleppe et al. (2001)
0	0.1270(112)	0	5.6807(3)	11.5243(6)	8.2515(6)	540.20(5)	90.090(7)	SX	XRD	Holl et al. (2008)
0	0.1400(100)	0	5.674(1)	11.477(2)	8.235(1)	536.2(1)	90.21(1)	SX	XRD EMPA SIMS	Kudoh and Inoue (1999) *

Appendix Table S5. (continued)

Fe/(Mg+Fe)	H$_2$O (pfu)	Fe^{3+}/$\sum$Fe	Unit cell edge lengths			Volume	Angle[a]	Sample[b]	Methods[c]	Reference
x	y	z	a (Å)	b (Å)	c (Å)	V (Å^3)	β (°)			
0	0.1598(136)	0	5.6803(7)	11.5235(15)	8.2503(11)	540.05(9)		SX	XRD	Ye et al. (2009)
0	0.1820(126)	0	5.679(1)	11.520(9)	8.252(3)	539.9(7)		P	XRD SIMS	Inoue et al. (2004)
0	0.1894(187)[e]	0	5.663(1)	11.546(2)	8.247(4)	539.2(5)		SX	XRD EMPA SIMS[e]	Kudoh et al. (1996)
0	0.1894(187)	0	5.675(3)	11.569(5)	8.244(4)	541.3(4)	90.09(4)	SX	XRD EMPA SIMS	Kudoh and Inoue (1999)
0	0.2113(303)	0	5.662(1)	11.577(2)	8.242(2)	540.3(2)		SX	XRD	Ye et al. (2010)
0	0.2186(174)	0	5.6646(4)	11.5818(5)	8.2388(3)	540.52(5)	90.051	P	XRD	Griffin et al. (2013)
0	0.2404(187)	0	5.6654(1)	11.6041(20)	8.2412(9)	541.79(11)	90.176	P	XRD	Griffin et al. (2013)
0.054(2)	0.1754(141)	0.96(5)[f]	5.6715(7)	11.5820(16)	8.2576(11)	542.43(12)	90.397(9)	SX	XRD SIMS MS[f]	Smyth et al. (1997)
0.074(1)	0.0610(72)	0.150(2)	5.6972(2)	11.4903(3)	8.2655(2)	541.1(3)		SX	XRD EMPA SIMS MS	Smyth et al. (2014)
0.10(1)	0.0203(20)		5.7045(4)	11.4765(4)	8.2707(4)	541.46(5)		SX	XRD FTIR	Chang et al. (2015)
0.11(1)	0.1539(153)	0.11(6)	5.6918(10)	11.5276(10)	8.2641(8)	542.23(12)		SX	XRD SIMS MS	Mao et al. (2011)
0.11(1)	0.1593(139)	0.11(6)	5.6929(2)	11.5275(2)	8.2648(1)	542.37(2)		SX	XRD SIMS MS	Chang et al. (2015)
0.112(2)	0.0192(18)	0.15(3)	5.7069(7)	11.4736(8)	8.2740(8)	541.77(9)	90.048(6)	SX	XRD EMPA FTIR MS	This study
0.150(2)	0.0778(33)	0.150(2)	5.7059(3)	11.5315(6)	8.2901(5)	545.47(5)		SX	XRD EMPA SIMS MS	Smyth et al. (2014)
0.222(4)	0.1176(149)	0.19(2)	5.711(2)	11.586(2)	8.293(2)	548.71(15)	90.138(9)	SX	XRD FTIR MS	Mrosko et al. (2015)
0.226(3)	0.0599(26)	0.247(2)	5.7194(3)	11.5434(6)	8.3030(5)	548.18(5)		SX	XRD EMPA SIMS MS	Smyth et al. (2014)
0.262(5)	0.0482(27)	0.275(5)	5.7237(1)	11.5302(4)	8.3034(2)	547.99(3)		SX	XRD EMPA SIMS MS	Smyth et al. (2014)
0.300(3)	0.0653(36)	0.303(3)	5.7243(2)	11.5804(4)	8.3108(3)	550.92(3)		SX	XRD EMPA SIMS MS	Smyth et al. (2014)
0.301(4)	0.0281(54)	0.310(3)	5.7238(3)	11.5844(7)	8.3124(5)	551.17(6)		SX	XRD EMPA SIMS MS	Smyth et al. (2014)
0.327(4)	0.0404(9)	0.300(3)	5.7276(2)	11.5680(5)	8.3072(3)	550.41(4)		SX	XRD EMPA SIMS MS	Smyth et al. (2014)

Notes: No entry implies that the respective information was not available.

[a] For monoclinic unit cell.

[b] SX single crystal, P powder.

[c] XRD X-ray diffraction, EMPA electron microprobe analysis, MS Mössbauer spectroscopy, FTIR Fourier transform infrared absorption spectroscopy, SIMS secondary ion mass spectrometry, ND neutron diffraction, NMR nuclear magnetic resonance.

[d] Fe^{3+}/$\sum$Fe adopted from Fei et al. (1992).

[e] Hydrogen concentration adopted from Inoue et al. (1995).

[f] Fe^{3+}/$\sum$Fe adopted from McCammon et al. (2004).

* Not included in multi-end member analysis.

Appendix Table S6. Reanalyzed second-order Birch-Murnaghan equation of state parameters for wadsleyites of different compositions

Fe/(Mg+Fe)	H_2O (pfu)	$Fe^{3+}/\sum Fe$	Unit cell edge lengths			Volume	Isothermal bulk modulus		
x	y	z	a_0 (Å)	b_0 (Å)	c_0 (Å)	V_0 (Å^3)	K_0 (GPa)	K_0^R (GPa)	K_0^V (GPa)
0		0	5.73(2)	11.50(5)	8.31(5)	541.5(23)	131.1(155)	95.4(177)	99.4(164)
0		0	5.696(1)	11.453(1)	8.256(1)	538.59(12)		174.3(49)	176.0(33)
0		0	5.6850(7)	11.4406(13)	8.2377(13)	535.75(13)	160.3(26)	159.5(24)	163.9(25)
0		0					168.7(20)		
0	0	0				535.8(2)		168.6(23)	170.1(22)
0		0					164.7(20)		
0		0					170.7(20)		
0		0	5.6972(4)	11.4605(7)	8.2558(7)	539.03(12)	182.4(14)	182.0(8)	187.1(9)
0		0				537.6(1)	171.4(20)		
0		0					168.9(19)		
0.075(10)			5.705(2)	11.450(4)	8.258(3)	539.4(4)		167.4(13)	170.2(13)
0.075(10)			5.705(2)	11.450(4)	8.258(3)	539.4(4)		167.4(13)	170.2(13)
0.08(1)		0.08(2)^d	5.6984(5)	11.4431(10)	8.2611(11)	538.67(11)	168.8(25)	167.8(22)	174.2(23)
0.08(1)							169.5(12)		
0.091(3)							164.4(1)		
0.091(3)							164.4(1)		
0.12(1)							170.7(20)		
0.13(1)						542.0(3)	170.0(7)		
0.16(1)		0.08(2)^d	5.7062(5)	11.4566(10)	8.2705(10)	540.65(12)	164.4(24)	164.1(20)	169.4(20)
0.25(1)		0.08(2)^d	5.7122(7)	11.4887(14)	8.2870(15)	543.81(13)	165.3(27)	164.3(28)	169.2(29)
0.25(1)		0.08(2)^d	5.7188(5)	11.5093(10)	8.3002(10)	546.30(16)	186.6(20)	186.0(12)	191.7(12)
1		0.28(2)	5.8496(11)	11.8554(19)	8.3774(16)	580.97(30)	176.7(32)	176.5(20)	177.8(21)
0	0.0004(1)	0	5.6982(8)	11.4394(16)	8.2573(16)	538.22(11)	173.0(16)	172.1(22)	177.6(23)
0	0.0288(30)	0	5.6941(2)	11.4597(3)	8.2556(2)	538.70(3)		163.0(15)	165.2(13)
0	0.0295(29)	0	5.7019(9)	11.4650(17)	8.2478(17)	539.15(12)	164.9(12)	164.5(17)	168.7(17)
0	0.0649(61)	0	5.6888(6)	11.4830(8)	8.2523(6)	539.08(8)		159.3(19)	160.7(7)
0	0.0649(58)	0	5.6888(6)	11.4830(8)	8.2523(6)	539.08(8)		158.2(10)	160.0(9)
0	0.0908(83)	0	5.6803(9)	11.5190(19)	8.2496(18)	539.77(9)	159.5(9)	159.0(17)	163.2(17)
0	0.1270(112)	0	5.6722(26)	11.5535(71)	8.2494(58)	540.33(15)	160.8(12)	157.6(46)	163.0(48)
0	0.1270(114)	0	5.6807(3)	11.5243(6)	8.2515(6)	540.20(5)		147.0(9)	148.8(9)
0	0.1894(187)	0	5.6614(13)	11.5526(33)	8.2437(27)	539.01(23)	157.1(23)	155.4(25)	158.8(26)
0	0.1894(187)	0	5.6653(38)	11.5557(86)	8.2473(90)	539.79(88)	145.0(77)	142.8(70)	149.2(72)
0	0.2113(303)	0	5.6766(27)	11.5699(52)	8.2503(49)	541.74(40)	146.7(12)	145.8(14)	148.1(14)
0.10(1)	0.0203(20)	0				541.97(22)	165.7(8)		
0.11(1)	0.1539(153)	0.11(6)	5.6918(10)	11.5276(10)	8.2641(8)	542.23(12)		154.1(12)	155.8(8)
0.11(1)	0.1593(139)	0.11(6)				543.46(19)	153.2(6)		
0.112(2)	0.0192(18)	0.15(3)	5.7077(3)	11.4759(6)	8.2754(7)	542.03(7)	169.3(5)	168.6(5)	173.8(5)

Notes: No entry implies that the respective information was not available. See supplemental online material[1] for further information on data

[a] SX single crystal, PX polycrystal, P powder.

[b] HP-XRD high-pressure X-ray diffraction, BS Brillouin spectroscopy, UI ultrasonic interferometry, RUS resonant ultrasound spectroscopy.

[c] MA multi-anvil press, PC piston cylinder press, DAC diamond anvil cell with pressure medium: ME methanol ethanol, MEW methanol

[d] $Fe^{3+}/\sum Fe$ adopted from Fei et al. (1992).

* Included in multi-end member analysis.

Appendix Table S6. (continued)

k_{10} (GPa)	k_{20} (GPa)	k_{30} (GPa)	Sample[a]	Method[b]	Environment[c]	Pressure P_{MAX} (GPa)	Reference
388(94)	264(66)	243(93)	P	HP-XRD	MA	9.6	Mizukami et al. (1975)
576(14)	608(29)	424(12)	SX	BS		0	Sawamoto et al. (1984) *
544(14)	547(14)	384(10)	SX	HP-XRD	DAC	4.5	Hazen et al. (1990) *
			PX	UI	MA	12.5	Li et al. (1996)
557(13)	577(12)	416(9)	SX	BS	DAC (Ar/ME/He)	14.2	Zha et al. (1997) *
			PX	UI	PC MA	14.5	Fujisawa (1998)
			PX	UI HP-XRD	MA	7.0	Li et al. (1998)
625(5)	621(5)	438(3)	SX	HP-XRD	DAC (ME)	10.1	Hazen et al. (2000a) *
			PX	UI HP-XRD	MA	7.1	Li et al. (2001)
			PX	RUS		0	Isaak et al. (2007)
563(6)	623(6)	386(4)	SX	BS		0	Sinogeikin et al. (1998) *
563(6)	623(6)	386(4)	SX	BS	DAC (MEW)	17.7	Wang et al. (2014)
575(13)	602(13)	391(9)	SX	HP-XRD	DAC	4.5	Hazen et al. (1990) *
			PX	RUS		0	Isaak et al. (2010)
			PX	RUS		0	Katsura et al. (2001)
			PX	RUS		0	Mayama et al. (2004)
			PX	UI	MA	9.6	Li and Liebermann (2000)
			PX	UI HP-XRD	MA	12.4	Liu et al. (2009)
592(12)	543(11)	390(8)	SX	HP-XRD	DAC	4.5	Hazen et al. (1990) *
548(16)	582(17)	393(11)	SX	HP-XRD	DAC	4.5	Hazen et al. (1990) *
634(7)	647(7)	444(5)	SX	HP-XRD	DAC (ME)	10.1	Hazen et al. (2000a) *
502(10)	598(12)	500(10)	SX	HP-XRD	DAC (ME)	9.0	Hazen et al. (2000b) *
594(13)	595(13)	409(9)	SX	HP-XRD	DAC (MEW)	7.3	Holl et al. (2008) *
563(9)	566(9)	386(2)	SX	BS		0	Mao et al. (2008b) *
543(9)	575(10)	400(7)	SX	HP-XRD	DAC (MEW)	9.0	Holl et al. (2008) *
535(7)	537(7)	393(9)	SX	BS	DAC (MEW)	12.0	Mao et al. (2008a) *
541(5)	543(5)	380(3)	SX	BS		0	Mao et al. (2008b) *
569(10)	513(9)	387(7)	SX	HP-XRD	DAC (MEW)	8.6	Holl et al. (2008) *
615(30)	456(23)	396(20)	SX	HP-XRD	DAC (MEW)	9.6	Holl et al. (2008)
516(5)	497(4)	350(2)	SX	BS		0	Mao et al. (2008b) *
568(16)	463(13)	398(11)	P	HP-XRD	DAC (MEW)	8.5	Yusa and Inoue (1997) *
534(43)	481(39)	328(28)	SX	HP-XRD	DAC (ME)	6.8	Kudoh and Inoue (1998) *
467(8)	496(8)	370(6)	SX	HP-XRD	DAC (Ne)	61.3	Ye et al. (2010) *
			SX	HP-XRD	DAC (Ne)	31.9	Chang et al. (2015)
559(6)	492(5)	375(4)	SX	BS	DAC (MEW)	12.2	Mao et al. (2011) *
			SX	HP-XRD	DAC (Ne)	31.9	Chang et al. (2015)
576(3)	586(3)	402(2)	SX	HP-XRD	DAC (Ne)	20.0	This study *

treatment.

ethanol water, Ar argon, He helium, Ne neon.

Appendix Table S7.

Calculated second-order Birch-Murnaghan equation of state parameters for wadsleyite
end members (Voigt model)

End member	Volume	Isothermal bulk and linear moduli				
	V_0 (Å^3)	K_0 (GPa)	k_{10} (GPa)	k_{20} (GPa)	k_{30} (GPa)	$K_0^{R\ a}$ (GPa)
Three-end-member model						
Mg_2SiO_4	538.5(2)	169(2)	577(10)	594(8)	403(7)	169(2)
Fe_2SiO_4	569.6(3)	193(17)	700(74)	682(58)	474(57)	200(13)
MgH_2SiO_4	547.5(19)	49(18)	183(91)	-92(67)	88(65)	–
Four-end-member model						
Mg_2SiO_4	538.5(2)	169(2)	578(10)	593(8)	403(6)	170(2)
Fe_2SiO_4	569.6(3)	200(27)	785(115)	752(88)	457(89)	209(21)
MgH_2SiO_4	547.5(19)	48(18)	182(93)	-87(66)	86(65)	–
Fe_3O_4	598.5(5)	135(72)	-47(263)	282(213)	592(237)	–

[a] $K_0^R = 1/(1/k_{10} + 1/k_{20} + 1/k_{30})$; not calculated for $k_{i0} < 0$.